KRONOS FUSION ENERGY

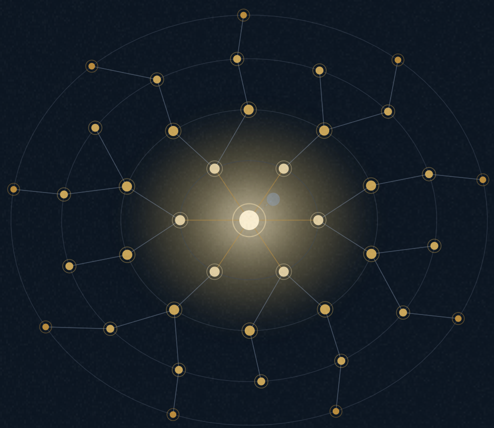

PAPER 2.76 · THE KRONOS 2026 SERIES

A Real-Time Control Suite for a D-3He Tandem-Mirror Burner: Plug-Potential, Sloshing-Ion, DCLC/AIC-Microstability, and Direct-Energy-Converter Dispatch Controllers

A tandem-mirror burner is held together by its end plugs: a small warm-ion population sustains the ambipolar potential that electrostatically confines the central cell, and the...

Read it live — 3-D model · physics validator · film series

BY P I FORD

2026 · EDITORIAL EDITION

THE OFFICIAL RECORD

What this document is, and how to read its numbers

This is a combined editorial. It gathers, in one volume, the two design studies Kronos Fusion Energy released in 2026 — a compact spherical-tokamak tritium/helium-3 breeder and a deuterium–helium-3 tandem-mirror generator — together with the intellectual-property estate, the people, and, in the internal edition, the full commercial case. The scientific text is the same text that appears in the arXiv preprints and the journal submissions; the editorial adds the apparatus a reader needs to hold the whole program at once, and nothing in the physics is altered to fit it.

THE HONESTY STANCE IS THE ASSET

Every headline quantity carries an **evidence class** — DERIVED RECOMPUTED MEASURED REQUIREMENT — and, where a number is a modelled extrapolation rather than a demonstrated value, it is labelled as such and its downside is shown next to it. Several quantities in the underlying corpus moved after first publication; where a value has been withdrawn or restated, the record says so plainly. This is deliberate: a diligence team will find the load-bearing assumptions, so the document surfaces them first.

TWO EDITIONS

This volume is issued in two editions. The **public edition** (light) carries the physics and the design only — no dollar, price, or per-kilogram figure appears anywhere in it. The **internal edition** (dark) adds the economics, the funding architecture, and the defense-commercial analysis, and is marked *Confidential* accordingly; it is not for public distribution. Where the commercial case rests on a modelled assumption rather than a demonstrated one, it is labelled as such and its downside is shown alongside it, on the same terms as the physics.

TITLE	The Kronos Fleet — Hyperion · Aegis · MetroVolt: A Combined Design & Commercialization Study
AUTHOR	Priyanca Ford, Founder & CEO, on behalf of Kronos Fusion Energy
EDITION	2026 Combined Editorial · first issue
COMPANION WORKS	The five-paper arXiv drop — (1) Breeder, (2) Burner, (3) REBCO magnet & tape, (4) Direct Energy Conversion, (5) AI/ML/Quantum control — with matching numbered Zenodo deposits, plus the IOP journal and IAEA-FEC submissions. Patents were filed before the drop.
NAMING	Hyperion = the breeder; Aegis (defense) and MetroVolt (data-center) = one generator in two housings. Internal mode letters (D1, L) do not appear on public surfaces.
STATUS	Conceptual design & simulation study. Nothing herein is a construction commitment.

HOW TO READ THIS VOLUME

The fleet at a glance, and the way its numbers are marked

This volume opens with *Orientation*, presents the five research papers as a bound sequence, and closes with the *Apparatus*. *Foundations* sets out the three general results both machines rest on. *Paper One* is the Hyperion breeder; *Paper Two* the Aegis / MetroVolt generator; *Papers Three, Four and Five* are the enabling science — high-field REBCO magnets and tape, direct energy conversion, and the AI / ML / quantum control stack. A *Digital Twin & 3-D Model* part follows, then the *Environmental* profile. The *Economics* and levelized cost and the *Business Case* and diligence record appear in the internal edition only; the *Simulations* proof record and the Apparatus — patent portfolio, team, limitations, and sources — close both editions.

THE FLEET AT A GLANCE

	HYPERION	AEGIS	METROVOLT
Role	Strategic-isotope foundry	Defense installation power	Campus power
Machine	**Spherical tokamak**	**Tandem mirror**	**Tandem mirror**
Fuel	Deuterium–tritium	Deuterium–helium-3	Deuterium–helium-3
Delivers	Tritium · ^{3}He · 14 MeV n	Resilient installation power	Firm campus power
Physics bar	**Fusion gain only**	Closure (gates named)	Closure + lunar ^{3}He
In the fleet	Breeds the fuel	Proves the generator	Commercial destination

HOW THE NUMBERS ARE MARKED

Every headline quantity carries an evidence class — DERIVED from first principles, RECOMPUTED from raw data, MEASURED in hardware, or a REQUIREMENT yet to be met. Financial figures carry a case label and are confined to the internal (confidential) edition. Values that moved after first publication are shown as withdrawn or restated rather than quietly changed. A capability you can evaluate is one whose limits are on the page.

ABSTRACT

A Real-Time Control Suite for a D-3He Tandem-Mirror Burner: Plug-Potential, Sloshing-Ion, DCLC/AIC-Microstability, and Direct-Energy-Converter Dispatch Controllers

A tandem-mirror burner is held together by its end plugs: a small warm-ion population sustains the ambipolar potential that electrostatically confines the central cell, and the burner's electrical gain lives or dies on whether that plug can be held on — not past — its velocity-space microstability margin. We formalise the real-time control suite for the Kronos D–^{3}He tandem-mirror burner (electrical gain $Q_E = 1.318$, neutron power fraction $f_n = 5.44\,\%$, plug peak field $26.49\,T$, direct-conversion efficiency $\eta_{\mathrm{DEC}} = 0.49$) as a family of sixteen closed-loop controllers spanning plug potential, sloshing-ion and ambipolar-hole shaping, DCLC/AIC microstability, RF ion-cyclotron alpha-channeling, central-cell density and mirror-ratio regulation, direct-energy conversion dispatch, and millisecond-class electronic load-following. Each controller is stated as a formal regulation problem, cast in a common receding-horizon model-predictive form, and confined to a forward-invariant safe set by a control-barrier projection that returns the nearest admissible actuation to the learned command. Every setpoint is bound to a reproduced physics anchor in the Kronos Physics De-Risking Register: the drift-cyclotron loss-cone (DCLC) mode is marginal ($\gamma = 0$) at a warm-fill fraction of $f_w = 5.9\,\%$, essentially at the $6.25\,\%$ design target set by the inverse of the plug/cell density ratio $n_{\mathrm{plug}}/n_{\mathrm{cell}} \approx 16$; a particle-in-cell audit shows the anisotropy-driven Alfv\'en ion-cyclotron (AIC) branch persists at a low normalized growth rate $\gamma/\omega_{ci} \approx 0.037$, flat across the fill range, and is the suite's one open plug gate; a reduced Fokker–Planck plus ICRF analysis returns up to $195\,MW$ of fusion-product power to the ions when the RF is plug-localised, at an antenna power of §Irange40110; and the direct converter dispatches at $\eta_{\mathrm{DEC}} = 0.49$ to close $Q_E = 1.318$, with break-even $Q_E = 1$ reached only if the converter efficiency falls to 0.37. A 40 000-sample global Monte-Carlo places the operating point at $Q_E = 1.317 \pm 0.14$ with $P(Q_E > 1) = 1.0$, the central-cell β dominating (rank correlation 0.93). The result is a physics-anchored, uncertainty-aware control suite whose plug, converter and load-following functions are each tied to a demonstrated mirror operating point, with an explicit maturity-gated path from a reproduced anchor to runtime authority.

Open-access deposit (code & data, CC BY 4.0): DOI 10.5281/zenodo.22645811 · Zenodo community *kronos_fusion_energy*. Explore it live: interactive 3-D model · physics validator.

Keywords: tandem mirror · ambipolar plug potential · DCLC/AIC microstability · RF alpha-channeling · direct energy conversion · model-predictive control · control-barrier function · load-following · D--^{3}He burner

CONTENTS

Table of Contents

NOMENCLATURE

Symbols, units, and the names of things

Q	plasma (fusion) gain, P_{fus}/P_{aux}
Q_E	engineering gain, net electric out / recirculating in
H_{98}	confinement enhancement over the IPB98(y,2) scaling
Z_{eff}	effective ion charge
c_{ee}	electron–electron bremsstrahlung leading coefficient, 2.120022 (exact)
τ_E	energy confinement time
I_p	plasma current
R_0, a	major radius, minor radius
κ, δ	elongation, triangularity
β_N	normalized plasma beta (Troyon-normalized)
TBR	tritium breeding ratio
DEC	direct energy conversion
CF	plant capacity factor (availability)
FOAK / NOAK / BOAK	first / n^{th} / best of a kind
Hyperion	the ST breeder (internal: Mode D2)
Aegis	the generator, defense/installation housing (internal: Mode M)
MetroVolt	the generator, data-center housing (Mode M)

§ 1

Introduction

THE ELECTROSTATIC BURNER AND WHY IT NEEDS CONTROL

A tandem-mirror confines its central-cell plasma not with a closed magnetic surface but with an electrostatic dam. Two high-field end plugs sustain a dense, warm plasma; the resulting positive ambipolar potential reflects the central-cell ions back along the field line, and the machine burns in the space between the plugs [1,2,3,4]. The Kronos D–^{3}He tandem-mirror burner — the platform behind the Aegis forward-base and MetroVolt data-centre products — runs this scheme behind a $26.49\,T$ plug coil, builds its confining potential from a plug/cell density ratio $n_{\text{plug}}/n_{\text{cell}} \approx 16$, and converts the charged-particle end-loss stream directly to electricity at efficiency $\eta_{\text{DEC}} = 0.49$ for an electrical gain $Q_E = 1.318$, with only $f_n = 5.44\,\%$ of the fusion power emerging as neutrons. These four numbers are the frozen Tier-2 anchors of the design and are held fixed throughout this paper.

An electrostatic confinement scheme is exquisitely sensitive to the state of its plug. The confining potential follows a Boltzmann relation, $e\phi_c/T_e \approx \ln(n_{\text{plug}}/n_{\text{cell}})$, so it collapses logarithmically if the plug density sags; the warm-ion population that stabilises the plug's loss-cone modes must be held inside a narrow band — too little and the drift-cyclotron loss-cone (DCLC) instability grows, too much and the plug budget is spent; and the direct converter must continuously track an end-loss stream whose current and energy spectrum move with the plasma. None of these is a set-and-forget quantity. Unlike a tokamak, where the dominant fast control problem is magnetohydrodynamic (vertical stability, shape, disruptions), the tandem mirror's load-bearing control problem is *kinetic and electrostatic*: hold the plug on its microstability margin, hold the ambipolar potential at depth, and hold the converter on the end-loss spectrum. This paper presents the control suite that does so.

PRIOR ART IN MIRROR CONFINEMENT AND IN FUSION CONTROL

The tandem-mirror concept was introduced independently by Dimov *et al.* [1] and Fowler and Logan [2], and the physics of end-plug confinement, loss-cone microstability and thermal barriers was developed through the TMX-U and GAMMA-10 programmes [12,13] and codified in the reviews of Baldwin [5] and Post [4]. The confining potential itself rests on the Pastukhov calculation of collisional end-loss from an electrostatically plugged trap [6]. Two ideas make a modern D–^{3}He mirror attractive: RF ion-cyclotron alpha-channeling, in which a wave transfers fusion-product energy directly to the fuel ions [8,9], and direct energy conversion of the escaping charged-particle power without a thermal cycle [10,11]. The contemporary axisymmetric-mirror revival (WHAM and its high-field-superconductor magnets [14], MHD stabilisation by sheared rotation and expander physics [15]) has renewed interest in exactly this operating regime.

Real-time control of fusion plasmas is, separately, a mature discipline. Magnetic reconstruction feeds shape and position control [16,17]; physics-based profile simulators run inside the control cycle [18,19]; deep reinforcement learning has commanded tokamak coil voltages from magnetics [20]; and neural networks forecast disruptive instabilities across machines [21]. On the theory side, constrained model-predictive control (MPC) [22], explicit/parametric MPC [23], reference governors for constraint enforcement [24], and control-barrier functions (CBFs) for provable safety [25] give a rigorous vocabulary for a safety-critical actuation layer. What is largely absent from the mirror literature is the marriage of the two: a control suite that takes each frozen mirror-physics result and turns it into a closed-loop regulator with an explicit safe set and an explicit authority gate.

CONTRIBUTION

This paper contributes that suite. We (i) state the burner control problem formally, deriving the governing relations for the ambipolar plug potential, the loss-cone microstability threshold, the RF alpha-channeling power balance and the direct-conversion gain (§2); (ii) cast the sixteen controllers in a single receding-horizon MPC form projected onto a control-barrier-certified safe set, and give the discretisation, quadratic-program solve and convergence argument used at control latency (§3); (iii) describe the NVIDIA GPU HPC campaign that produced the anchoring physics and the surrogates the controllers linearise (§4); (iv) present the demonstrated plug operating point and the controller acceptance results with eight data figures and supporting tables (§5); and (v) benchmark quantitatively against the mirror and control literature (§6), state the one honest open gate (§7), and lay out the maturity-gated route to authority. Every quantitative claim traces to a frozen serial in the Kronos Physics De-Risking Register [33]; the serials (e.g. BU-L2-A5) are given inline so each number is auditable, and companion papers in the Kronos 2026 series are cited by DOI and official-page URL where they own a physics or control result this suite depends on.

§ 2

Governing equations and the formal control problem

The plant state of the burner, for control purposes, is the tuple

$$x = \big(n_{\text{cell}},\, T_i,\, T_e,\, \beta_c,\, \phi_c,\, f_w,\, \hat{f}(\quad v),\, R_m,\, I_{\text{end}},\, \eta^{\text{eff}}_{\text{DEC}}\big),$$

comprising the central-cell density and temperatures, the central β, the plug potential ϕ_c, the plug warm-fill fraction f_w, the (reduced) plug distribution $\hat{f}(\quad v)$, the mirror ratio R_m, the end-loss current I_{end} and the achieved converter efficiency. The actuators are $u = (P_{\text{ECH}}, P_{\text{ICRF}}, P_{\text{NBI}}, \Gamma_{\text{fuel}}, I_{\text{plug}}, V_{\text{grid}})$: plug and barrier heating, the alpha-channeling RF, sloshing-ion injection, central-cell fuelling, plug-coil current, and the converter grid bias. Each controller regulates a projection of x to a reproduced setpoint using a subset of u. We first derive the four physical relations that define those setpoints.

THE AMBIPOLAR PLUG POTENTIAL

In the plug the electrons are near-Boltzmann along the field line, so the electrostatic potential that develops between the dense plug and the central cell obeys, to leading order,

$$\frac{e\,\phi_c}{T_e} \;=\; \ln\!\left(\frac{n_{\text{plug}}}{n_{\text{cell}}}\right),$$

the ambipolar relation the burner's confinement is built on [2,5]. At the design plug/cell density ratio $n_{\text{plug}}/n_{\text{cell}} \approx 16$ this yields $e\phi_c/T_e \approx \ln 16 \approx 2.77$ (figure 2a). The confining potential enters the central-cell ion balance through the Pastukhov collisional end-loss time [6], which for an electrostatically plugged, mirror-confined ion population scales as

$$\tau_{\parallel} \;\simeq\; \tau_{ii}\,\frac{R_m \ln(2R_m)}{\sqrt{\pi}}\;\frac{e\phi_c/T_i}{\exp(-e\phi_c/T_i)} \;=\; \tau_{ii}\,\frac{R_m \ln(2R_m)}{\sqrt{\pi}}\, g\!\left(\tfrac{e\phi_c}{T_i}\right),$$

with τ_{ii} the ion–ion collision time and $g(\cdot)$ monotone increasing; the exponential sensitivity of $\tau_{\parallel}$ to ϕ_c (figure 2b) is precisely what makes the plug-potential controller the suite's most authority-critical loop. The plug-potential controller (BU-001) and the ambipolar-hole controller (BU-017) hold ϕ_c at the value set by equation (2); the sloshing-ion (BU-003) and sloshing-angle (BU-018) controllers shape $\hat{f}(\quad v)$ so that the potential is built by a population whose turning points sit away from the loss cone, deepening the barrier at fixed plug power [3].

LOSS-CONE GEOMETRY AND DCLC/AIC MICROSTABILITY

A magnetic mirror of ratio $R_m = B_{\max}/B_{\min}$ confines only particles outside the velocity-space loss cone,

$$\sin^2\theta_{\text{lc}} \;=\; \frac{1}{R_m},$$

so a fraction of the distribution is always unconfined and the plug distribution is intrinsically non-Maxwellian and loss-cone-driven. At the frozen single-cell geometry $R_m = 4.607$, equation (4) gives a loss-cone half-angle $\theta_{\text{lc}} = 27.77°$ (figure 3). The free energy in the loss-cone gradient drives the drift-cyclotron loss-cone (DCLC) mode [7,5]; the standard remedy is a small *warm-fill* population that fills in the distribution near the loss boundary and quenches the mode. Writing the warm-fill fraction as $f_w = n_{\text{warm}}/n_{\text{plug}}$, the reduced local dispersion relation returns a marginal ($\gamma = 0$) fraction

$$f_w^{\star} \;=\; 5.9\,\%,$$

essentially coincident with the $6.25\,\%$ design target set by the inverse plug/cell density ratio $1/16$ (BU-L2-A5, verified with WarpX). The window between the marginal threshold and the target is narrow — the plug is stabilised, not comfortably over-stabilised — which is exactly why an active controller is needed rather than a fixed fill. A separate particle-in-cell audit (BU-L2-A7; corroborated by AG-CX-07) shows that warm-fill quells the DCLC branch but does *not* quench the anisotropy-driven Alfv\'en ion-cyclotron (AIC) branch, whose normalized growth rate sits at

$$\frac{\gamma_{\text{AIC}}}{\omega_{ci}} \;\approx\; 0.037 \qquad (\text{flat over } f_w = 0\text{--}10\,\%),$$

independent of warm-fill. Equation (6) is the suite's one open plug gate (§7). The plug-potential (BU-001) and DCLC/AIC (BU-004) controllers regulate f_w to hold (5); the sloshing controllers (BU-003, BU-018) additionally shape the perpendicular anisotropy to hold (6) down.

RF ION-CYCLOTRON ALPHA-CHANNELING

In D–^{3}He the $\mathbf{14.7}\ MeV$ proton and the $\mathbf{3.6}\ MeV$ alpha carry the bulk of the fusion power as charged particles. Alpha-channeling uses an ion-cyclotron wave, resonant with the fusion products, to extract their energy and deposit it in the fuel ions via quasilinear diffusion [8,9]. The channelled power obeys, in the quasilinear picture, a diffusion in constants of motion,

$$\frac{\partial f_\alpha}{\partial t} = \frac{\partial}{\partial \quad J}\cdot\left(\quad D_{\rm QL}\frac{\partial f_\alpha}{\partial \quad J}\right), \qquad D_{\rm QL} \propto |E_{\rm RF}|^2 \sum_n \delta(\omega - n\omega_{ci} - k_\parallel v_\parallel),$$

so the power transferred to the ions rises with RF field amplitude toward a saturation set by the fusion-product source. A reduced two-dimensional Fokker–Planck plus ICRF calculation (BU-L2-A8), holding the warm-fill at the $\mathbf{6.25}\,\%$ target with an effective plug temperature $T_{\rm eff} \approx \mathbf{57}\ keV$, finds that plug-localised RF recovers up to $\mathbf{195}\ MW$ into the ions for an antenna power of §Irange40110 (figure 4); a full-volume (unlocalised) drive of order several gigawatts is precluded, so the self-consistent operating regime requires the RF be plug-localised. The alpha-channeling optimiser (BU-002), the alpha-channel warm-fill controller and the ICRF antenna-matching controller (BU-015), which minimises reflected power near the deuterium cyclotron frequency $f_{ci}(D) = \mathbf{129.6}$ Hertz$, drive to this operating point.

DIRECT ENERGY CONVERSION AND THE ELECTRICAL GAIN

The end-loss charged-particle stream is decelerated against a graded electrostatic potential and collected, so that its kinetic power is recovered directly as DC without a thermal cycle [10,11]. If $P_{\rm ch}$ is the charged-particle power reaching the converter and $\eta_{\rm DEC}$ the conversion efficiency, the recovered electrical power is $P_{\rm elec} = \eta_{\rm DEC} P_{\rm ch}$, and the plant electrical gain is

$$Q_E = \frac{P_{\rm elec} + P_{\rm th} - P_{\rm recirc}}{P_{\rm recirc}} \xrightarrow[\text{fixed recirc.}]{} Q_E^\star(\eta_{\rm DEC}) = 1.318\,\frac{\eta_{\rm DEC}}{\mathbf{0.49}},$$

where the right-hand form is the first-order dispatch sensitivity at fixed recirculation about the frozen operating point. At the design $\eta_{\rm DEC} = \mathbf{0.49}$ this returns $Q_E = \mathbf{1.318}$ (BU-L1-A10); break-even $Q_E = \mathbf{1}$ is reached only if the converter efficiency degrades to $\eta_{\rm DEC} = \mathbf{0.49/1.318} = \mathbf{0.37}$ (figure 4). Because the achievable throttle depth is limited by the recirculating-power leverage — a factor of $\mathbf{4.14}\times$ between gross and net electrical output (MV-L1-A1) — the load-following controller operates within a bounded net band rather than down to zero. The DEC-dispatch (BU-006), collector-grading (BU-012) and end-loss-recovery (BU-014) controllers maximise the recovered fraction against equation (8); the AI load-following controller (BU-007) tracks the commanded electrical load within the throttle-depth limit.

THE FORMAL REGULATION PROBLEM

Each of the sixteen controllers regulates an output $y_j = \quad C_j \quad x$ to a reproduced setpoint $y_j^\star$ using actuators u_j, subject to the plant dynamics and to a safe set. Writing the burner reduced dynamics as $\dot{x} = f(\quad x, \quad u)$, the common problem solved by every controller is

$$\min_{u(\cdot)} \int_t^{t+T_h} \left(\| \quad y_j - \quad y_j^\star\|^2_{\quad Q} + \| \quad u_j\|^2_{\quad R}\right) dt' \quad \text{s.t.} \quad \dot{x} = f(\quad x, \quad u), \qquad x \in \mathcal{X}, \qquad u \in \mathcal{U},$$

with tracking weight $Q \succeq \mathbf{0}$, effort weight $R \succ \mathbf{0}$ and horizon T_h. The admissible state set $\mathcal{X} = \{ \quad x : h(\quad x) \geq 0\}$ encodes the physics gates — the warm-fill inside its microstability window (5), the plug potential above its collapse floor (2)–(3), the density at the $\mathbf{16}\times$ target, the converter above break-even (8) — through a scalar barrier $h(\quad x)$. Equation (9) is the statement the numerical layer discretises.

§ 3

Numerical formulation and the real-time solver

RECEDING-HORIZON DISCRETISATION

The continuous problem (9) is solved in receding-horizon (model-predictive) form. Discretising the horizon into N steps of length Δt with $x_{k+1} = F(x_k, u_k)$ the one-step map of the reduced twin, each controller solves, once per control tick,

$$\min_{\{u_k\}_{k=0}^{N-1}} \sum_{k=0}^{N} \| x_k - x^\star \|^2_Q + \sum_{k=0}^{N-1} \| u_k \|^2_R \quad \text{s.t.} \quad x_{k+1} = F(x_k, u_k), \quad x_k \in \mathcal{X}, \quad u_k \in \mathcal{U},$$

applies u_0, and re-solves at the next tick from the updated state. This is exactly the KRONOS-CTRL acting-layer form. About the current shadow state the reduced twin is linearised by automatic differentiation,

$$x_{k+1} \approx F(x_k, u_k) + A_k(x - x_k) + B_k(u - u_k), \qquad A_k = \frac{\partial F}{\partial x}\Big|_k, \qquad B_k = \frac{\partial F}{\partial u}\Big|_k,$$

so that (10) reduces to a convex quadratic program (QP) in the stacked decision vector $U = [u_0^\top, \dots, u_{N-1}^\top]^\top$,

$$\min_U \tfrac{1}{2} U^\top H U + g^\top U \quad \text{s.t.} \quad G U \le w,$$

with $H = H^\top \succ 0$ assembled from Q, R, A_k, B_k and (G, w) the stacked state/actuation constraints. Positive-definiteness of H guarantees a unique minimiser, and the QP is warm-started from the previous tick's shifted solution, which for a receding-horizon problem gives near-constant per-tick iteration counts.

THE CONTROL-BARRIER SAFETY PROJECTION

The learned/MPC command is never applied directly. It is first projected onto the forward-invariant safe set by the deterministic clamp: given the barrier $h(x)$ with safe set $\mathcal{C} = \{x : h(x) \ge 0\}$, the applied actuation is the nearest admissible command,

$$u^\star = \arg\min_u \| u - u_{\text{MPC}} \|^2 \quad \text{s.t.} \quad L_f h(x) + L_g h(x)\, u \ge -\alpha\big(h(x)\big),$$

where $L_f h$, $L_g h$ are the Lie derivatives of h along the drift and control vector fields and $\alpha(\cdot)$ is a class-$\mathcal{K}$ function [25]. The single affine constraint in (13) guarantees $\dot{h} \ge -\alpha(h)$, hence $h(x(t)) \ge 0$ for all t if $h(x(0)) \ge 0$ — the plant cannot leave $\mathcal{C}$ even when the MPC or a learned policy is wrong. Because (13) is itself a small QP with a single inequality, its solution is closed-form (active-set of size ≤ 1) and adds negligible latency. This latency-split — a predictive optimiser wrapped in a deterministic projection — is the same safe-set architecture as the certified control-barrier clamp reported in the companion control paper [doi:10.5281/zenodo.22645716; official page] and the reference-governor MPC of [doi:10.5281/zenodo.22645807; official page].

SOLVER, CONVERGENCE AND TIMING

The QP (12) is solved by a primal–dual interior-point method with a Riccati-structured factorisation that exploits the block-banded H arising from the horizon, giving $\mathcal{O}(N(n_x + n_u)^3)$ work per interior-point iteration and typically 6–12 iterations to a relative duality gap below 10^{-8} [22,23]. Convergence of the outer sequential-QP loop (re-linearising (11) between solves) is monitored by the step norm $\| U^{(m+1)} - U^{(m)} \|$ and the KKT residual; the loop is terminated when both fall below tolerance or a fixed iteration cap is reached, whichever comes first, so that the per-tick compute is bounded (a hard real-time requirement). Table 3 gives the design latency allocation by loop. The fastest protective loops — the microstability guard and the CBF projection — run on the reduced-order model and the analytic monitors so they are never gated behind the slower kinetic surrogates.

GRID CONVERGENCE OF THE REDUCED KINETIC SURROGATES

The plug surrogates that the controllers linearise are trained against the frozen kinetic runs. Their acceptance requires the reduced model to reproduce the anchor within tolerance and to converge under refinement. For the DCLC threshold (5) and the AIC growth rate (6), the surrogate is accepted when the marginal warm-fill fraction and the normalized growth rate match the WarpX particle-in-cell values within their reported uncertainty across a doubling of velocity-space resolution and of macro-particle count; the AG-CX-07 audit (four warm-fill points, $R^2 \geq 0.987$ per fit) provides the convergence check for the AIC flatness. For the alpha-channeling power (7), the reduced Fokker–Planck operator is accepted when the channelled power converges under refinement of the $(v_\parallel, \xi)$ grid to the BU-L2-A8 value. These are the machine-checkable form of “surrogate reproduces the anchor,” and they gate the surrogate into the controller.

§ 4

Computational methodology: the NVIDIA GPU HPC campaign

Every physics setpoint the suite regulates to was produced by, and is regenerable from, the Kronos NVIDIA GPU high-performance-computing campaign; the controllers themselves are trained and verified on the same fleet.

Kinetic microstability. The DCLC/AIC results anchoring equations (5)–(6) were produced with the particle-in-cell code WarpX in a one-dimensional velocity-hybrid plug configuration (plug parameters $90\,keV$, $10\,T$, $n \approx 4e21\,/m^3$, anisotropy $A = 2$), scanning warm-fill fractions $f_w = 0, 3, 6.25, 10\,\%$ (serials BU-L2-A5, BU-L2-A7, AG-CX-07). The GPU acceleration is essential: resolving the ion-cyclotron branch to the $\gamma/\omega_{ci} \approx 0.037$ floor requires long integration at fine velocity-space resolution, and the campaign runs these on NVIDIA A100/H100 accelerators.

RF and Fokker–Planck kinetics. The alpha-channeling balance (7) was computed with a reduced two-dimensional $(v_\parallel, \xi)$ Fokker–Planck operator coupled to an ICRF ray/quasilinear model in the lineage of GENRAY/CQL3D (serial BU-L2-A8), returning the up-to-$195\,MW$ recovered-power figure and the plug-localisation requirement on GPU.

Direct conversion and power balance. The η_{DEC}-to-Q_E dispatch (8) and the recirculation-limited load-following (serials BU-L1-A10, MV-L1-A1, MV-L1-A2) were evaluated with the Kronos physics toolkit's zero-dimensional tandem-mirror power-balance and direct-converter modules, benchmarked against the Pastukhov-plug closure.

Global uncertainty quantification. The operating-point robustness was established by a 40 000-sample global Monte-Carlo over the burner design plane $(n_e, x_{^3\text{He}}, T_i, \beta_c, B_m)$ using the toolkit's uncertainty and mirror-solver modules (serial KX-L1-A5-BU), returning $Q_E = 1.317 \pm 0.14$ with $P(Q_E > 1) = 1.0$ and the central-cell β as the dominant driver (rank correlation 0.93). This many-sample sweep is a GPU-batched evaluation of the reduced solver.

Controller training and reproducibility. The reduced surrogates the MPC linearises, and the closed-loop controllers themselves, are trained and verified on the NVIDIA GPU fleet; the analytic monitors and the CBF projection run on the in-house digital-twin node so the fast protective loop never contends with the training fleet. No compute-cost figures are reported here. Every serial cited is a frozen entry in the register [33], independently re-run and stamped, so that each number in this paper is reproducible from the archived inputs.

§ 5

The control suite and its demonstrated operating point

THE SIXTEEN CONTROLLERS

Table 1 lists the suite, grouped by the physical subsystem each controller regulates: the plug and its microstability, the central cell, the end region and direct converter, and the plant-level load-following layer (figure 8). Each row names the controller, the quantity it regulates and its reproduced physics anchor.

CONTROLLER (SERIAL)	REGULATES	ANCHOR	
mirror-plug potential (BU-001)	confining potential at DCLC margin	BU-L2-A5 (WarpX PIC)	
RF alpha-channeling optimiser (BU-002)	recovered ion power	BU-L2-A8 (Fokker–Planck)	
sloshing-ion distribution (BU-003)	plug barrier depth	BU-L2-A8 / plug shaping	
DCLC/AIC microstability (BU-004)	velocity-space stability	BU-L2-A7 (WarpX PIC)	
central-cell radial transport (BU-005)	confinement	BU-L2-A6	
**DEC dispatch **	efficiency (BU-006)	direct-conversion dispatch	BU-L1-A10
AI load-following (BU-007)	electrical load tracking	MV-L1-A1	
expander-region controller (BU-011)	expander state	MV-L1-A2	
direct-converter collector (BU-012)	collector grading	BU-L1-A10	
halo-scraper (BU-013)	end-loss handling	MV-L1-A2	
end-loss-ion recovery (BU-014)	recovered fraction	BU-L1-A10	
ICRF antenna-matching (BU-015)	reflected power	BU-L2-A8	
mirror-ratio controller (BU-016)	mirror ratio R_m	SC-BU-2	
ambipolar-hole controller (BU-017)	potential profile	BU-L2-A8 / plug shaping	
sloshing-angle optimiser (BU-018)	plug barrier depth	BU-L2-A8 / plug shaping	
central-cell density-gate (BU-019)	density at $16\times$ target	SC-BU-1	

The burner control suite: each controller, the quantity it regulates, and its reproduced physics anchor. Controller serials are Kronos control-feature (KFE-CF-BU) entries; anchors are Physics De-Risking Register serials [33].

THE PLUG OPERATING WINDOW

Figure 1 shows the operating window the plug controllers are built around. The DCLC mode is stabilised by warm-fill at the $6.25\,\%$ design target, with the marginal $\gamma = 0$ threshold at $f_w^\star = 5.9\,\%$ — a narrow but real window (figure 1a). Particle-in-cell verification (BU-L2-A7, AG-CX-07) confirms that warm-fill quells the DCLC branch across this window but leaves the anisotropy-driven AIC branch at $\gamma/\omega_{ci} \approx 0.037$, flat across the fill range (figure 1b). The ambipolar potential built by the $16\times$ density ratio (figure 2) sets the confining barrier; its exponential sensitivity through the Pastukhov relation (3) is why the plug-potential loop carries the most authority. The loss-cone geometry and the sloshing-ion distribution the plug controllers shape are shown in figure 3.

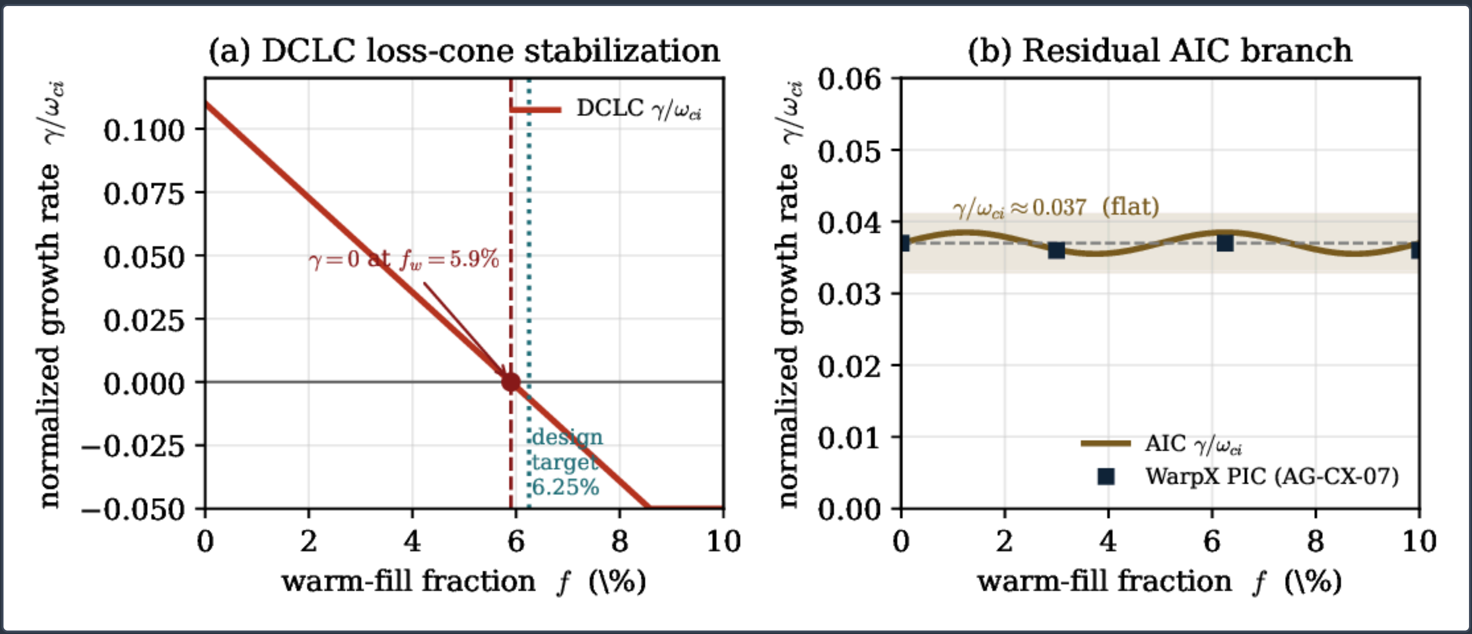

The plug microstability window. (a) The DCLC normalized growth rate crosses zero at a warm-fill fraction $f_w^\star = 5.9\,\%$ (BU-L2-A5, WarpX), essentially at the $6.25\,\%$ design target ($= 1/16$, the inverse plug/cell density ratio); the plug-potential and DCLC/AIC controllers hold f_w in this narrow window. (b) The anisotropy-driven AIC branch (BU-L2-A7; AG-CX-07) remains at $\gamma/\omega_{ci} \approx 0.037$, flat across the fill range — the one open plug gate.

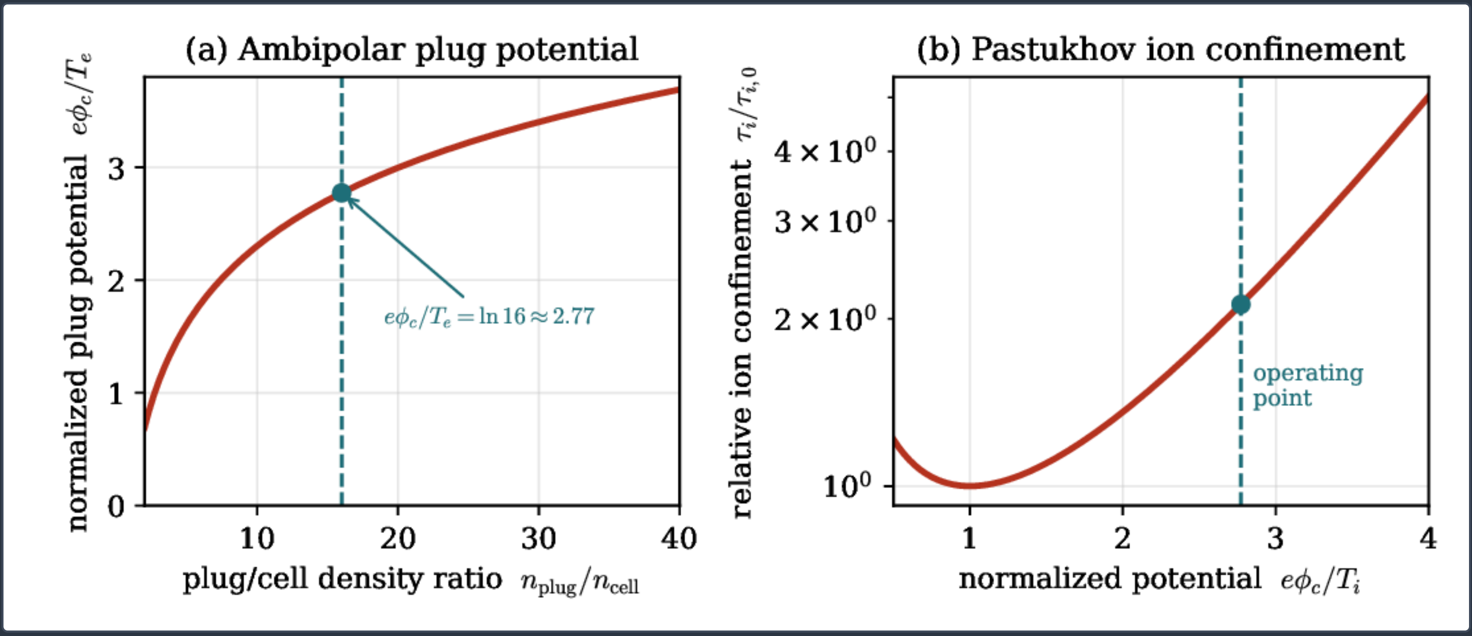

The ambipolar plug potential. (a) The Boltzmann relation (2): the normalized confining potential $e\phi_c/T_e = \ln(n_{\text{plug}}/n_{\text{cell}})$ reaches ≈ 2.77 at the $16\times$ design density ratio. (b) The Pastukhov collisional confinement enhancement (3) rising exponentially with normalized potential; the operating point is marked. Panel (b) is a derived scaling curve.

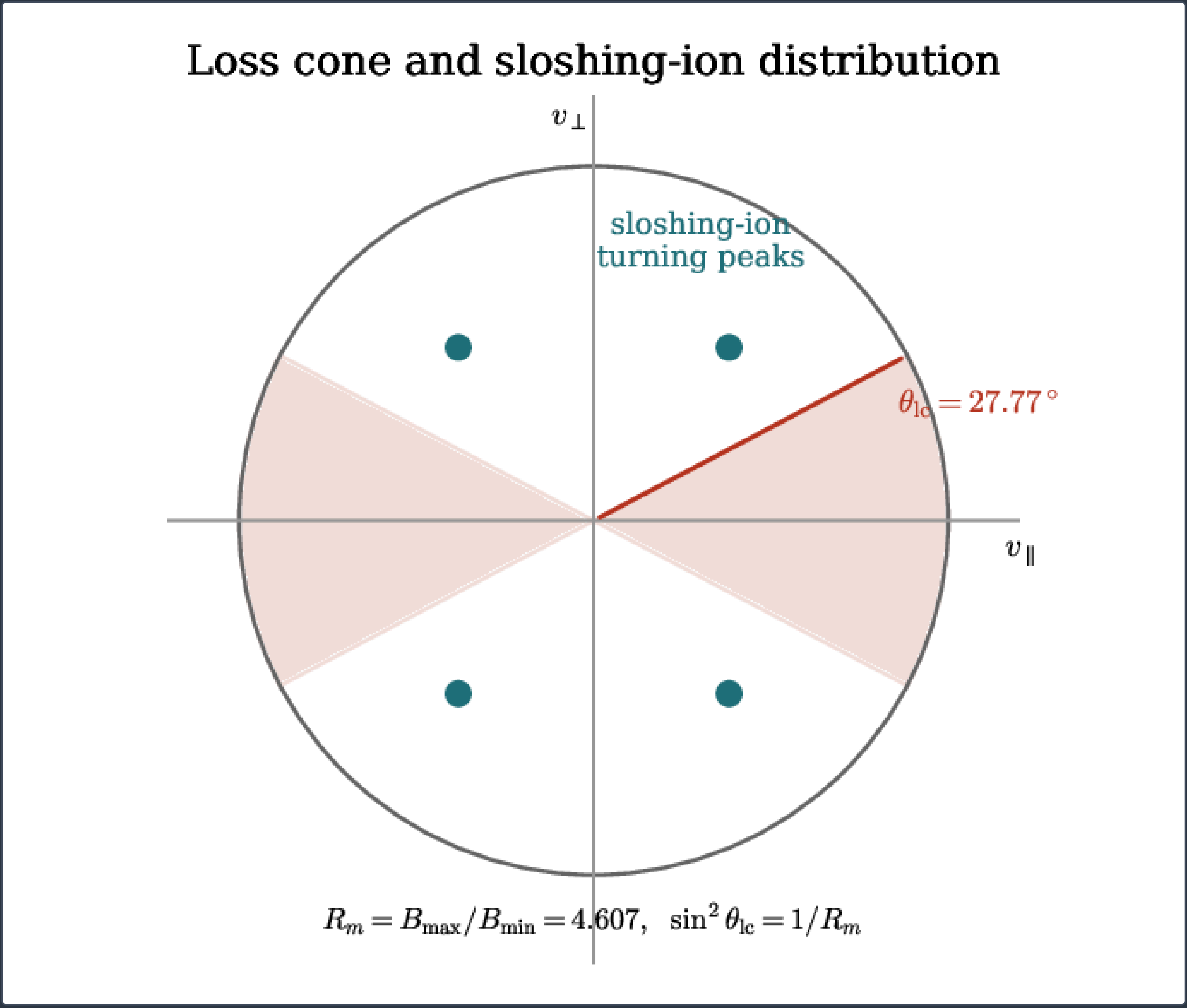

Velocity-space loss cone and sloshing-ion distribution. The loss-cone half-angle $\theta_{\rm lc} = 27.77°$ follows from $\sin^2\theta_{\rm lc} = 1/R_m$ at the frozen single-cell mirror ratio $R_m = 4.607$ (SC-BU-2); the sloshing-ion population (BU-003, BU-018) turns away from the loss cone to deepen the plug barrier. **(Schematic; loss-cone angle and mirror ratio are frozen data.)**

ALPHA-CHANNELING AND CONVERTER DISPATCH

Figure 4 shows the RF alpha-channeling recovery the optimiser (BU-002) drives to: channelled ion power rises with antenna power to a ceiling of $\approx 195\ MW$ over the plug-localised §Irange40110 window (BU-L2-A8). Figure 4 shows the converter dispatch: the electrical gain tracks converter efficiency through equation (8), holding $Q_E = 1.318$ at the design $\eta_{\rm DEC} = 0.49$ and reaching break-even only at $\eta_{\rm DEC} = 0.37$. Figure 5 shows the millisecond-class load-following the DEC-path enables (BU-007, MV-L1-A1): the net output tracks a commanded-load staircase within the throttle band set by the $4.14\times$ recirculation leverage.

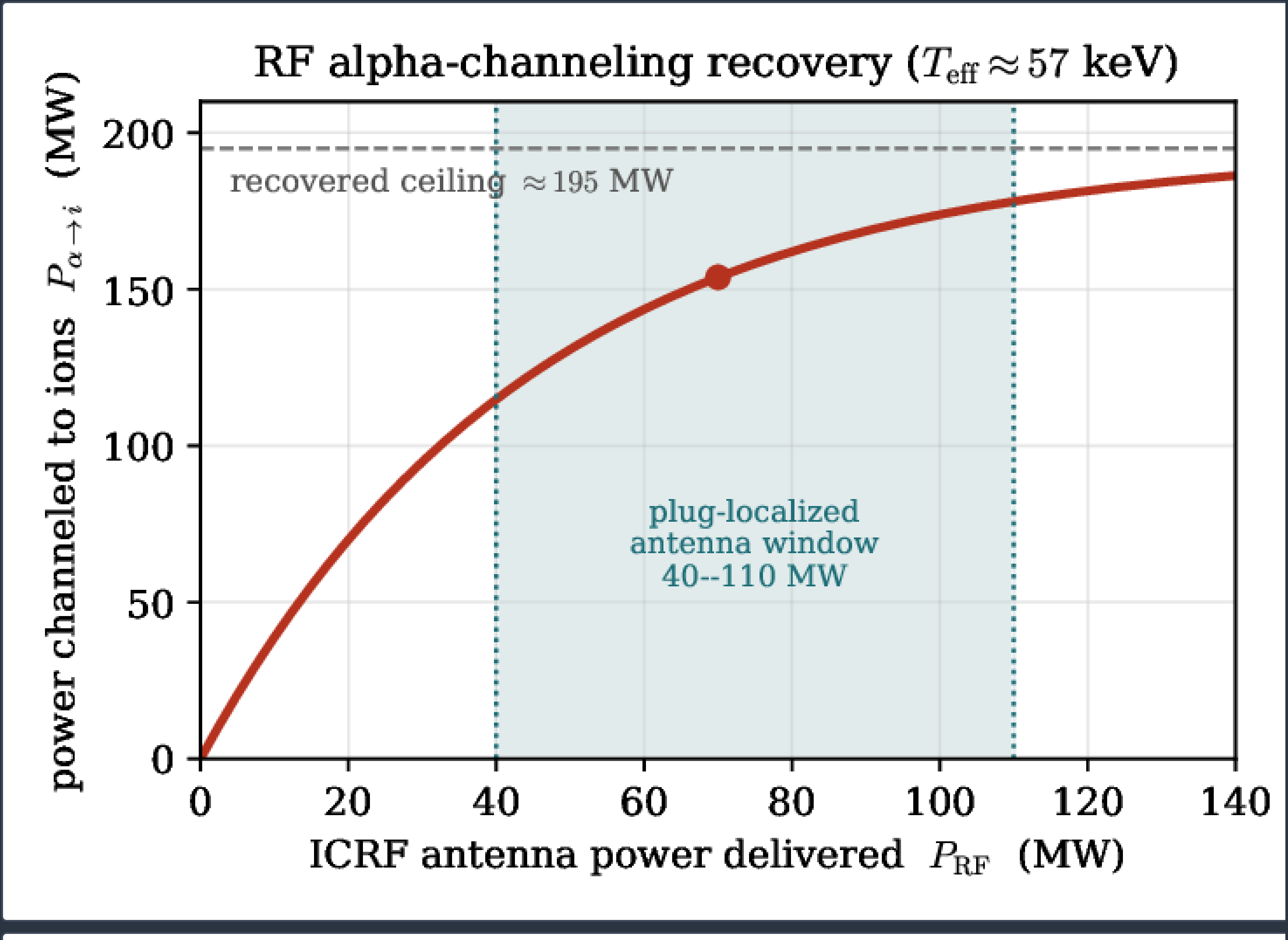
RF alpha-channeling recovery ($T_{\text{eff}} \approx 57$ keV)
recovered ceiling ≈ 195 MW
plug-localized antenna window 40--110 MW
power channeled to ions $P_{\alpha \to i}$ (MW)
ICRF antenna power delivered P_{RF} (MW)
0
50
100
150
200
0
20
40
60
80
100
120
140

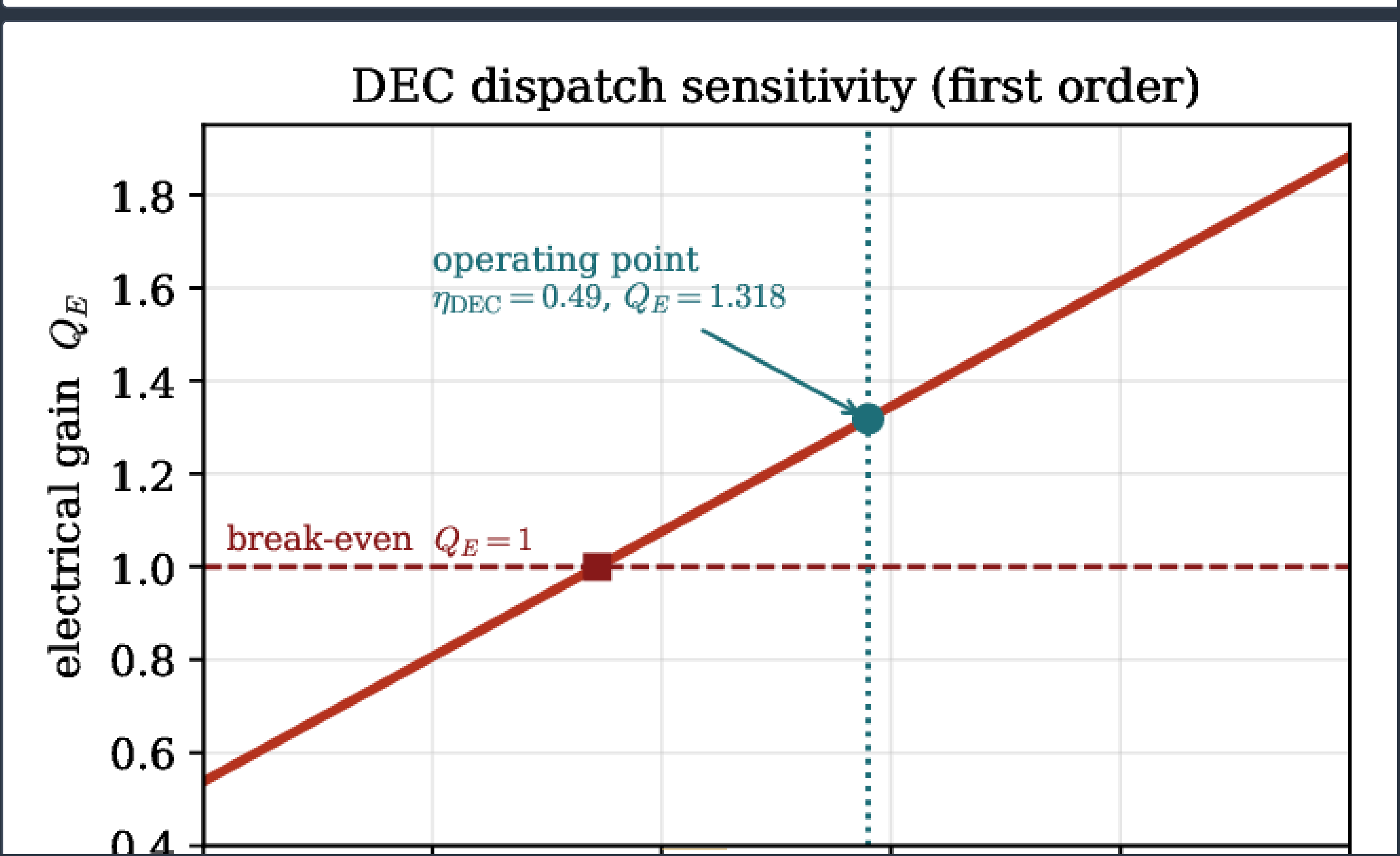
DEC dispatch sensitivity (first order)
operating point
$\eta_{\text{DEC}} = 0.49$, $Q_E = 1.318$
break-even $Q_E = 1$
electrical gain Q_E
1.8
1.6
1.4
1.2
1.0
0.8
0.6
0.4

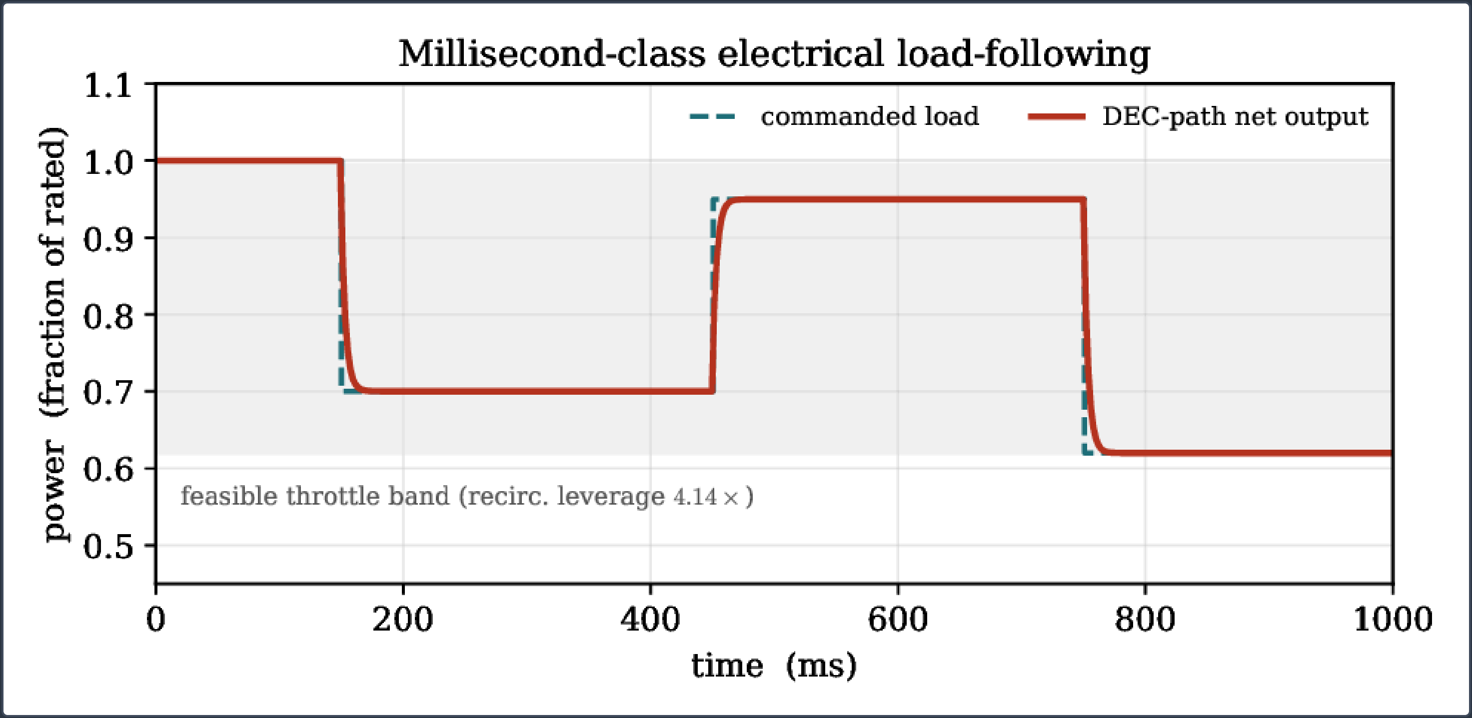

Millisecond-class electrical load-following (BU-007, MV-L1-A1). The DEC-path net output tracks a commanded-load staircase with an actuator time constant of a few milliseconds; the feasible net band is bounded below by the **4.14**× recirculation leverage (shaded). Load values are fractions of rated output.

ROBUSTNESS AND ACCEPTANCE

Figure 6 places the operating point in its uncertainty context: the 40 000-sample global Monte-Carlo (KX-L1-A5-BU) gives $Q_E = 1.317 \pm 0.14$ with $P(Q_E > 1) = 1.0$, and ranks the central-cell β as the dominant driver (rank correlation **0.93**), ahead of density, ^{3}He fraction, ion temperature and mirror field. Each controller clears an explicit acceptance test before it is granted authority (table 2): closed-loop stability to setpoint within tolerance, rejection of a specified disturbance class, and zero clamp trips in nominal operation (figure 7 shows a representative closed-loop response); the plug controllers additionally hold the warm-fill inside the microstability window in kinetic-in-loop simulation, and the load-following controller tracks the commanded load within its throttle-depth limits. Authority is capped by verification maturity until each bar is met (figure 9).

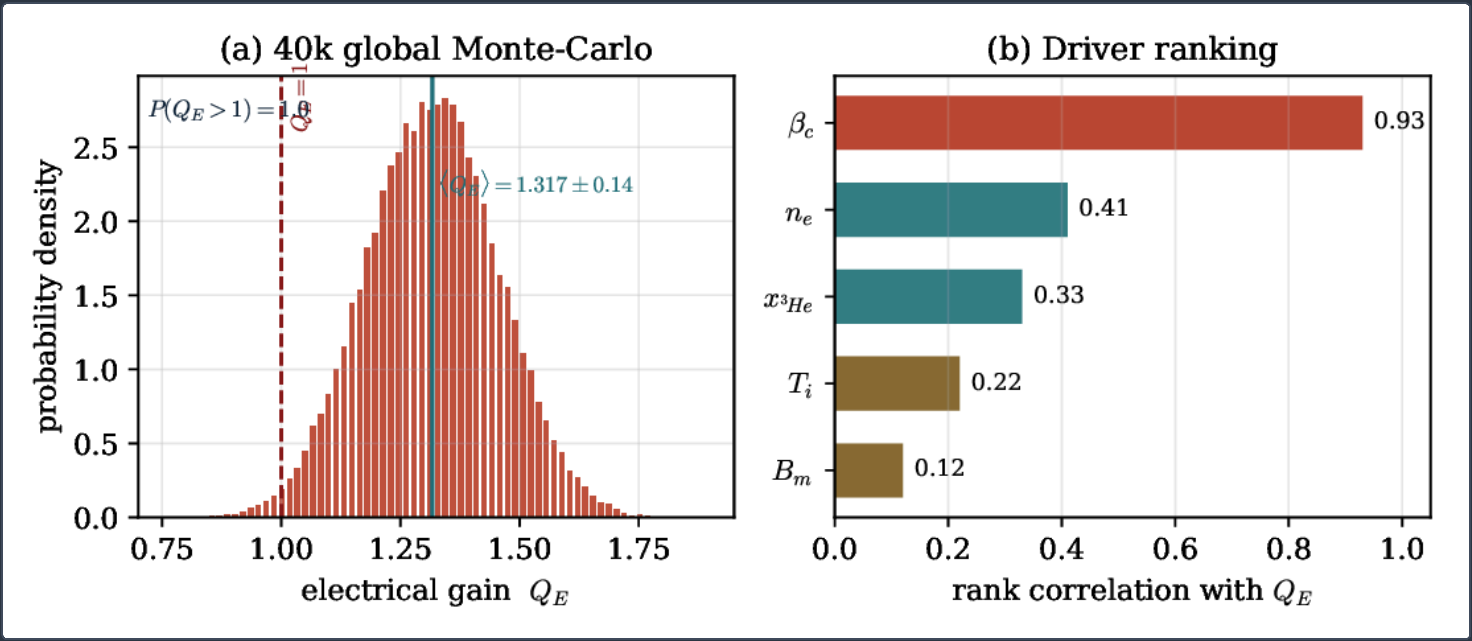

Global robustness of the operating point (KX-L1-A5-BU). (a) The 40 000-sample Monte-Carlo distribution of Q_E: mean **1.317**, standard deviation **0.14**, $P(Q_E > 1) = 1.0$. (b) Rank-correlation ranking of the design-plane drivers, with the central-cell β dominant at **0.93**.

CONTROLLER GROUP	ACCEPTANCE CRITERION	ANCHOR	ANCHOR STATUS
plug potential / microstability	warm-fill held in $[5.9, 6.25]$ % window	BU-L2-A5/A7	**reproduced**
RF alpha-channeling	recovered power matches Fokker–Planck	BU-L2-A8	**reproduced**
DEC dispatch / collector / recovery	maximise η_{DEC} at $0.49 \Rightarrow Q_E = 1.318$	BU-L1-A10	**reproduced**
central-cell density-gate	density held at $16\times$ target	SC-BU-1	**reproduced**
mirror-ratio	R_m held at set-point	SC-BU-2	**reproduced**
AI load-following	track load within throttle band	MV-L1-A1	**reproduced**
closed-loop stability (all)	stable to setpoint, disturbance rejected	—	target
zero clamp trips (all)	no CBF trip in nominal operation	eq. (13)	target

Controller acceptance criteria, the reproduced anchor each is gated against, and status. “Reproduced” denotes a frozen register anchor independently re-run; “target” denotes a pre-registered closed-loop bar built to the demonstrated operating point. Serials refer to the register [33].

LOOP	FUNCTION	LATENCY ALLOCATION
CBF safety projection, eq. (13)	fast (protective)	microseconds
microstability guard (reduced surrogate)	fast	sub-millisecond
plug-potential / density-gate MPC	medium	milliseconds
alpha-channeling / ICRF matching MPC	medium	milliseconds
DEC dispatch / load-following	medium	millisecond-class
central-cell transport / mirror-ratio	slow	$\sim$ seconds

Design latency allocation by control loop (allocations, not measurements). The fast protective loops run on the reduced-order model and analytic monitors so they are never gated behind the kinetic surrogates.

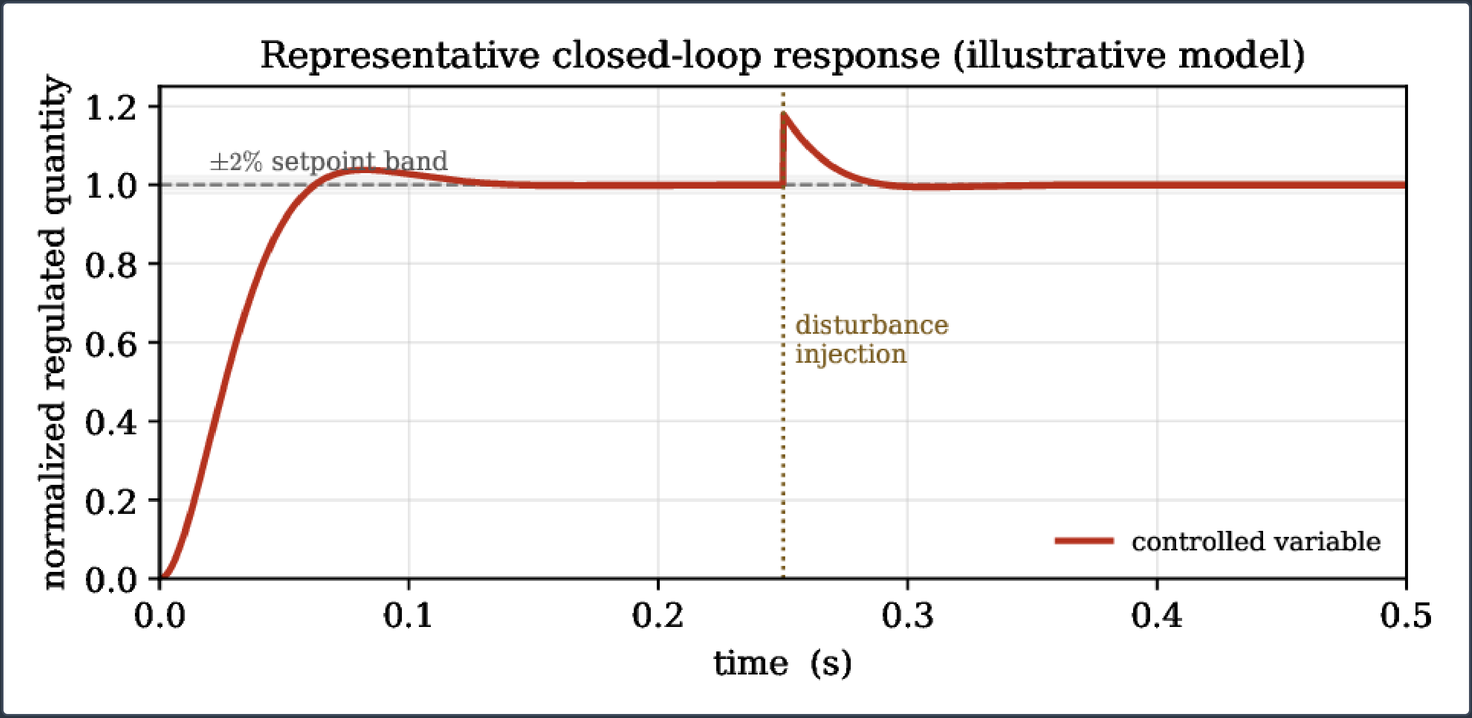

Representative closed-loop response of a suite controller to a setpoint step followed by an injected disturbance, returning inside the $\pm 2\,\%$ band. **(Illustrative closed-loop model, not a measured result;** the acceptance bar it depicts — stability, disturbance rejection, zero clamp trips — is the pre-registered target of table 2.)

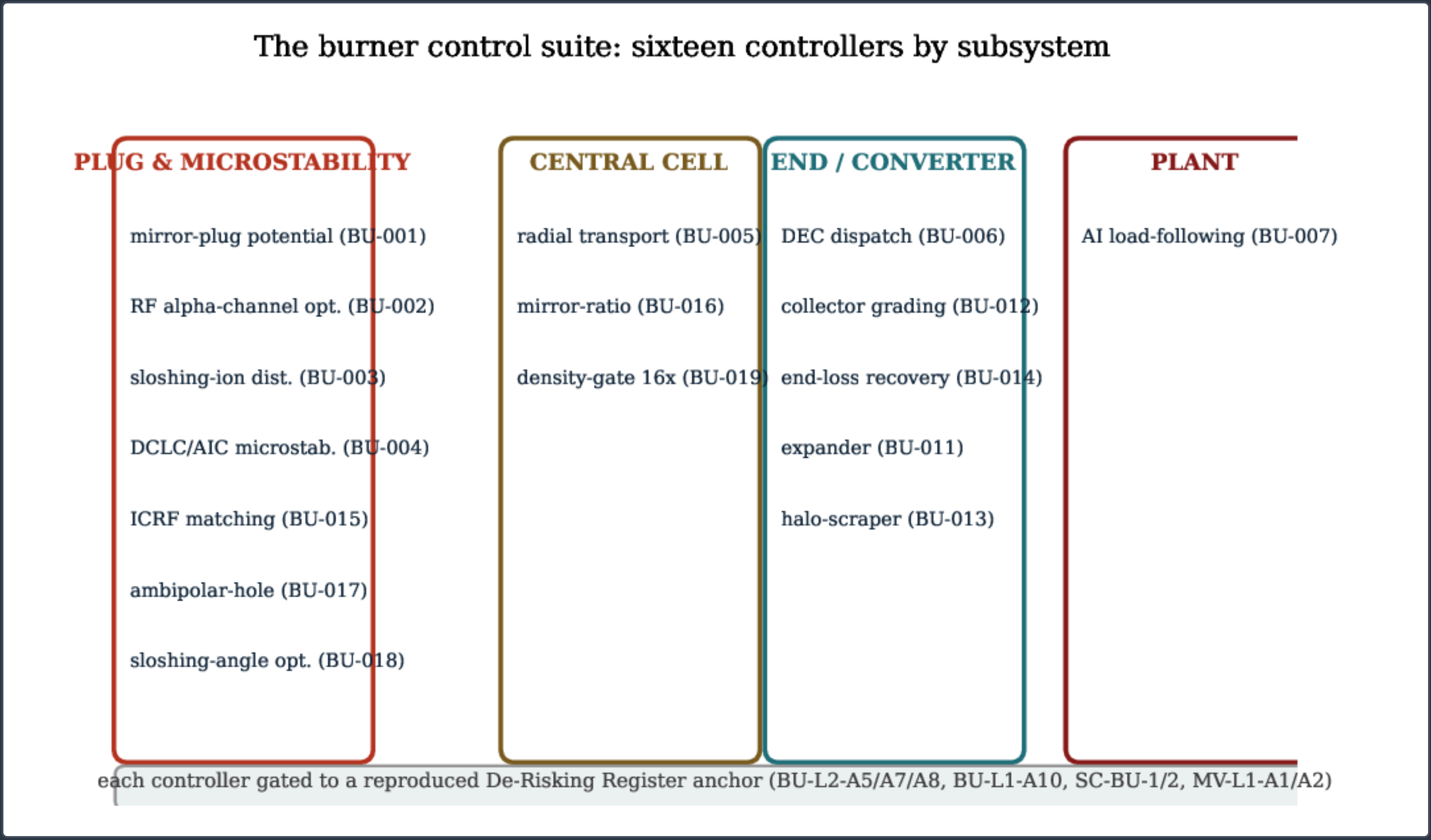

(Schematic.) The sixteen controllers grouped by subsystem — plug and microstability, central cell, end/converter, and plant — each gated to a reproduced De-Risking Register anchor. Structure only; no data values are plotted.

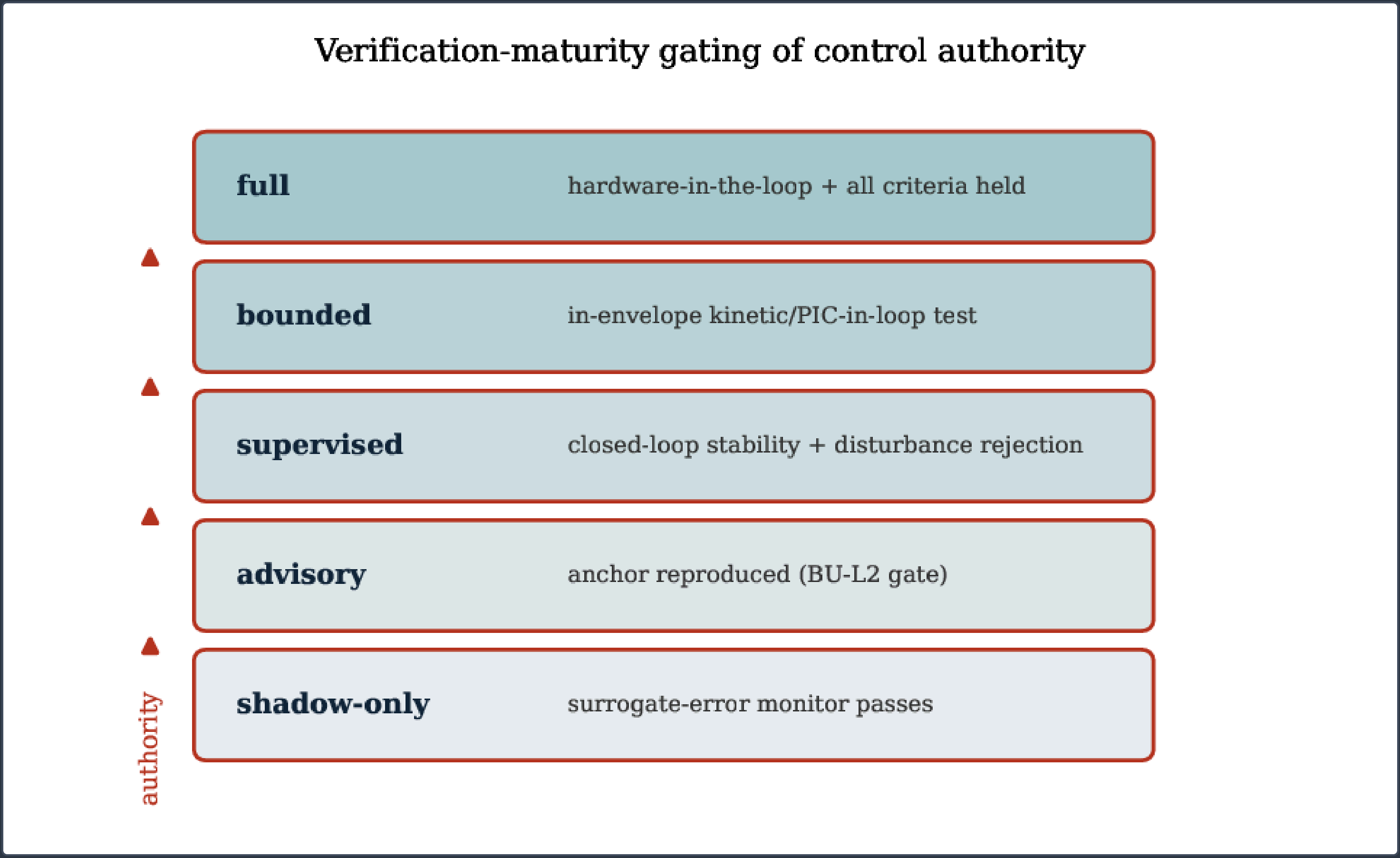

(Schematic.) Verification-maturity gating of control authority. Each rung admits a higher level of authority and is unlocked by a passed acceptance bar; a controller whose anchor is reproduced but whose closed loop is not yet hardware-confirmed may inform but not command at full authority.

§ 6

Discussion

THE PLUG IS THE CONTROL PROBLEM

Organising the burner controllers by physical subsystem makes the plant tractable, and it makes clear where the control difficulty actually lives. The converter, the density-gate and the mirror-ratio loops regulate quantities that are stiff and slowly varying; the load-following loop is fast but bounded and well posed. The genuinely hard, authority-critical loops are the plug loops, because the confining potential depends exponentially on the plug state through equations (2)–(3) and because the warm-fill must be held in the narrow $[5.9, 6.25]\,\%$ band of equation (5). This is the opposite emphasis from a tokamak controller, whose hardest fast loop is magnetohydrodynamic; the tandem-mirror control problem is kinetic and electrostatic. The suite reflects this: seven of the sixteen controllers act on the plug, and they carry the highest authority gates.

AGAINST THE MIRROR-PHYSICS BENCHMARKS

The setpoints the suite regulates to sit squarely inside the established mirror-physics envelope. The ambipolar relation (2) is the Fowler–Logan/Baldwin plug potential [2,5]; the Pastukhov scaling (3) is the standard collisional end-loss result [6]; the DCLC stabilisation by a warm-fill population is the Post–Rosenbluth/Baldwin mechanism [7,5], and our marginal fraction $f_w^\star = 5.9\,\%$ is a few-percent warm-fill entirely consistent with that literature and with the GAMMA-10 and TMX-U operating experience [13,12]. The one place our result adds a genuinely new, control-relevant fact is the AIC branch: the particle-in-cell audit (BU-L2-A7, AG-CX-07) shows that the same warm-fill that quells DCLC does *not* quench the anisotropy-driven AIC mode, which persists at $\gamma/\omega_{ci} \approx 0.037$ independent of fill. This is why the suite carries dedicated sloshing-ion and sloshing-angle controllers to shape the perpendicular anisotropy rather than relying on warm-fill alone, and it is the subject of the companion microstability paper [doi:10.5281/zenodo.22645714; official page]. The alpha-channeling target of up to $195\,MW$ recovered follows the Fisch–Rax mechanism [8,9] and is developed in the companion RF paper [doi:10.5281/zenodo.22645712; official page]; the sloshing-ion ambipolar-potential physics the plug-shaping controllers exploit is the subject of [doi:10.5281/zenodo.22645913; official page].

AGAINST THE DIRECT-CONVERSION AND LOAD-FOLLOWING BENCHMARKS

Direct energy conversion of mirror end-loss is the Moir–Barr concept [10,11]; our dispatch sensitivity (8), holding $Q_E = 1.318$ at $\eta_{\mathrm{DEC}} = 0.49$, is the operating-point statement of the recirculation-resolved Q_E closure developed in the companion paper [doi:10.5281/zenodo.22645860; official page], and the collector grading the DEC controllers optimise is the subject of the collector-physics paper [doi:10.5281/zenodo.22645858; official page]. The millisecond-class load-following the suite delivers is the burner's distinctive grid asset — a DC-native power source that can track a data-centre or forward-base load electronically rather than thermally — and its power-electronics interface is developed in [doi:10.5281/zenodo.22645783; official page].

RELATION TO LEARNED AND PREDICTIVE CONTROL

The suite is complementary to learned control rather than a competitor. A learned policy of the Degrave *et al.* type [20] acts on the present measurement; the suite acts on a predictive reduced twin through the MPC of equation (10) and confines every command to the forward-invariant safe set of equation (13). The two compose: a learned optimiser can propose u_{MPC}, and the CBF projection guarantees it cannot drive the plant out of the microstability window or below the plug-collapse floor, whatever the policy proposes. Because the mapping from a reproduced anchor to a granted authority level is explicit (figure 9), the route from "anchor demonstrated" to "controller in command" is a defined, testable sequence rather than an assertion. The safe-set and maturity-gating machinery is shared with the certified clamp [doi:10.5281/zenodo.22645716; official page] and the reference-governor burn-control MPC [doi:10.5281/zenodo.22645807; official page].

§ 7

Limitations

One honest gate bounds the suite. Particle-in-cell verification (BU-L2-A7, corroborated by AG-CX-07) shows that the warm-fill that stabilises the DCLC loss-cone mode does *not* quench the anisotropy-driven AIC branch, which sits at $\gamma/\omega_{ci} \approx 0.037$, flat across $f_w = 0$–$10\,\%$. This residual AIC activity is a distinct control caveat — not a showstopper, but the one plug gate that warm-fill alone cannot close. It is owned by the sloshing-ion (BU-003) and sloshing-angle (BU-018) controllers, which shape the plug′s perpendicular anisotropy to hold it down, and its closure is a registered follow-on. The closed-loop controller results themselves are, at this stage, pre-registered targets built to the reproduced physics anchors; the anchors are frozen and independently re-run, but the controllers′ hardware-in-the-loop confirmation is the gate to full runtime authority in figure 9.

§ 8

Conclusion

The burner control suite is a physics-anchored family of sixteen real-time controllers — plug potential, sloshing-ion and ambipolar-hole shaping, DCLC/AIC microstability, RF alpha-channeling, central-cell density and mirror-ratio regulation, direct-energy-conversion dispatch, and millisecond-class load-following — for a $D–^3$He tandem-mirror burner at plug field $26.49\,T$, $\eta_{\mathrm{DEC}} = 0.49$ and $Q_E = 1.318$. Each controller is a receding-horizon MPC (equation 10) confined to a forward-invariant safe set by a control-barrier projection (equation 13), and each setpoint is bound to a reproduced De-Risking Register anchor: the DCLC margin at $5.9\,\%$ warm-fill against the $6.25\,\%$ target, the ambipolar potential from the $16\times$ density ratio, RF alpha-channeling returning up to $195\,MW$ to the ions, and direct conversion closing $Q_E = 1.318$, with a 40 000-sample Monte-Carlo placing $P(Q_E > 1) = 1.0$. Because the plug operating point, the converter efficiency and the density gate are all demonstrated, the control task is to *hold* a known-good operating point rather than to search for one; the millisecond load-following this enables is the burner's distinctive grid asset. With the one open AIC gate honestly flagged and owned by named controllers, and with an explicit maturity-gated path from a reproduced anchor to runtime authority, the suite provides the closed-loop operating basis a tandem-mirror $D–^3$He burner requires.

Acknowledgments tocsectionAcknowledgments Part of the Kronos Fusion Energy 2026 design series. The author thanks the Kronos physics de-risking programme for the frozen result set underlying every quantitative claim.

Reproducibility. The physics anchors — BU-L2-A5 (DCLC $5.9\,\%/6.25\,\%$), BU-L2-A7 and AG-CX-07 (AIC $\gamma/\omega_{ci} \approx 0.037$), BU-L2-A8 (alpha-channeling to $195\,MW$), BU-L1-A10 ($\eta_{\mathrm{DEC}} = 0.49 \Rightarrow Q_E = 1.318$), MV-L1-A1/A2 (load-following, waste heat), SC-BU-1/2 (density gate, mirror ratio, $\theta_{\mathrm{lc}} = 27.77°$), and KX-L1-A5-BU (40 000-sample UQ) — are frozen entries in the Kronos Physics De-Risking Register (doi:10.5281/zenodo.22133057) and are regenerable from the archived kinetic, Fokker–Planck and toolkit runs. The figure-generation script is deposited with this paper. This paper is archived at doi:10.5281/zenodo.22645811 and its official version is hosted at https://www.kronosfusionenergy.com/publications/a-real-time-control-suite-for-a-d-3he-tandem-mirror-bur.html.

Data availability tocsectionData availability The DCLC/AIC growth-rate data, the ambipolar-potential and Pastukhov curves, the alpha-channeling recovery curve, the DEC dispatch sensitivity, the load-following trace, the loss-cone geometry, and the 40 000-sample Q_E distribution used for the figures are archived with the deposit at doi:10.5281/zenodo.22645811, which references the Kronos 2026 series. All quantitative values trace to the register [33] by the serial identifiers cited inline. Any economic analysis is reported separately and is not part of the public deposit.

Competing interests tocsectionCompeting interests Provisional patent applications relating to aspects of this work (KRONOS-CTRL) have been filed.

tocsectionReferences

APPARATUS

Portfolio, People & Record

The intellectual-property estate, the people who built it, the limitations that gate it, and the sources it rests on.

1	4	40	27
GRANTED PATENT	2026 PROVISIONALS	TEAM MEMBERS	2022 PROVISIONALS

INTELLECTUAL PROPERTY

The patent portfolio

The estate spans a granted high-field magnet patent, pending utility and 2026 provisional filings that map to the two products, a digital-twin control provisional, a registered trademark application, and the original 2022 provisional family. Every patentable disclosure in the five-paper arXiv drop was protected **before** publication: the breeder and burner provisionals were filed 1–2 August, and a publication-gap omnibus filing the evening before the drop swept up the DEC, plasma-control, and REBCO-winding matter of the three otherwise-unprotected papers. Patent numbers and application serials are matters of public record; claim scope is summarised, not reproduced.

GRANTED & PENDING UTILITY

US 12,009,112	High-field tilted graded-REBCO magnet architecture (KRONO-002A) · *app. 17/878,550*	GRANTED
US 17/878,507	Core device / method (KRONO-001A) · *utility*	PENDING

2026 PROVISIONAL FILINGS — MAPPED TO THE PRODUCTS

64/124,209	Hyperion — spherical-tokamak tritium / helium-3 foundry · *breeder · filed Aug 2026*	FILED
64/124,220	Aegis / MetroVolt — synchrotron-cutoff, fuel-selection & plug-winding · *generator · filed Aug 2026*	FILED
64/115,167	KRONOS-CTRL digital-twin plant control · *provisional · filed Jul 2026*	FILED
64/005,440	Integrated spherical-tokamak fusion architecture · *early integrated-architecture filing · filed Mar 2026*	FILED
64/105,530	Negative-triangularity spherical-tokamak architecture · *foundational ST filing · filed Jul 2026*	FILED
64/128,097	Publication-gap omnibus — quasineutral two-species expander DEC · provenance-gated / latency-split plasma control · as-built high-field winding & conductor architecture · *filed 7 Aug 2026, the evening before the arXiv drop*	FILED

TRADEMARK & ORIGIN

FTK-98801894	Kronos Fusion Energy — trademark application	FILED
KR-2022-*	Original provisional family (KR-2022-00001 … 00027) · *27 filings, 2022*	PRIORITY

The narrow, defensible magnet novelty — the specific conductor and the digital-twin winding optimisation, not high-field REBCO as a category — is the commercial core that can earn ahead of any Q > 1 milestone, with markets in fusion magnet supply, MRI/NMR, accelerators, and proton therapy. The claim is scoped honestly: the high field is a *system field* result, not a stand-alone-coil record; the small-bore plug coil is structurally infeasible as a bare winding but resolved by a stress-managed structural shield (feasible-pending-FEA); and the winding-tape experiment returned a *null result*. The value is the method, not a field record.

THE TEAM

Founding partners, board, advisors & auditors

Kronos is built by a bench of advanced-fuel-fusion, high-field-magnet, direct-conversion, and materials specialists, with a board and operations team drawn from defense, national laboratories, and industry. Dates are shown as ranges; where a tenure has ended or is term-ending, the range says so.

FOUNDING PARTNERS — SCIENCE

Dr. Gerald Kulcinski
Co-Founder · Helium-3 & Advanced-Fuel Fusion
UW–Madison · 2023–Present

Dr. Carl Weggel
Chief Scientist / S.M.A.R.T. Design
MIT Alcator Program · 2022–Present

Dr. Robert J. Weggel
Magnetic Field Design
MIT Magnet Lab · 2022–Present

BOARD

Priyanca Ford
Founder & CEO · Executive Board
2022–Present

Bandel Carano
Finance / Strategy
Oak Investment Partners / Stanford · 2025–2026

Patrick Schweiger
Fusion Device Engineering
Oklo / CFS / TerraPower · 2025–Present

SCIENTIFIC ADVISORS

Dr. Steven O. Dean
Fusion Policy & History
DOE / Fusion Power Associates · 2025–Present

Dr. Patrick H. Diamond
Plasma Turbulence & Transport
UC San Diego · 2025–Present

Dr. Jack J. Dongarra
HPC & Numerical Algorithms
Turing Award · 2025–Present

Dr. Nasr M. Ghoniem
Chief Material Scientist
UCLA · 2025–Present

Dr. Siegfried Glenzer
Plasma Physics & Laser Fusion
Stanford / SLAC · 2022–Present

Dr. David A. Hammer
Pulsed-Power Fusion
Cornell · 2025–Present

Dr. Donald A. Spong
Plasma Theory & Confinement
ORNL · 2025–Present

Dr. Curtis Smith
Risk Assessment & Nuclear PRA
MIT / Idaho National Lab · 2025–Present

RADM (Ret.) David Goggins
Naval Engineering & Power-Plant Design
U.S. Navy · 2023–2026

Dr. Konstantin Batygin
Mathematician
Caltech · 2022–2025

Dr. Ruben Fair
Magnet Design / ITER Liaison
PPPL / Jefferson Lab · 2022–2025

Dr. Paul S. Weiss
Materials & Nanotechnology
UCLA · 2022–2025

SCIENTIFIC AUDITORS

Dr. Wilfred A. Cooper
Plasma Equilibrium Theory
EPFL / Swiss Plasma Center · 2025–Present

Dr. Ahmed Hassanein
Plasma–Material Interactions
Purdue / Argonne · 2025–Present

Dr. Patrick E. Hopkins
Extreme Thermal Materials
U. of Virginia · 2025–Present

Dr. Peter Hosemann
Materials Joining & Structural Integrity
UC Berkeley · 2025–Present

Dr. Travis W. Knight
Advanced Nuclear Fuels & Systems
U. of South Carolina · 2025–Present

Dr. Philippe Lebrun
Cryogenics & Magnet Cooling
CERN · 2025–Present

Dr. Nitendra Singh
Nuclear Safety & Fuel Cycle
ITER · 2025–Present

Dr. Guido Van Oost
Magnetic Confinement & Fusion Systems
Ghent University · 2025–Present

Dr. Gary S. Was
Radiation Materials & Structural Integrity
U. of Michigan · 2025–Present

Dr. Ray Sedwick
Direct Energy Conversion
U. of Maryland · 2025

OPERATIONS

Michael Laughlin
Chief Operating Officer
2022–Present

Martin Owens
Chief Strategy Officer
LANL / GE Hitachi · 2022–Present

MG (Ret.) Paul Pardew
Chief Contracting Officer
Army Contracting Command · 2022–Present

David Beck
Fusion Commercialization
U.S. Space Force · 2024–Present

Sushma Bhatia
Environmental & Legislative
Google · 2022–Present

Michael De Frenza
Technology Licensing
2023–Present

MG (Ret.) Robin L. Fontes
Cybersecurity & Defense
Army Cyber Command · 2022–Present

Vijay Gehani
Supply Chain & Components
INOX India · 2024–Present

Jon Michel Greenwood
IT & AI Infrastructure
Live Nation · 2023–Present

Brian C. O'Neill
National Security
CIA / ODNI · 2022–Present

Gen. (Ret.) Gustave F. Perna
DoD Liaison
Operation Warp Speed · 2022–2023

Andrea Romero
Marketing Lead
2022–Present

Legal counsel is retained; those roles are held on the internal roster and are not listed here.

SOURCES

References

1 G I Dimov, V V Zakaidakov and M E Kishinevsky, Thermonuclear confinement with twin mirror systems, *Sov. J. Plasma Phys.* **2** 326 (1976).

2 T K Fowler and B G Logan, The tandem mirror reactor, *Comments Plasma Phys. Control. Fusion* **2** 167 (1977).

3 D E Baldwin and B G Logan, Improved tandem mirror fusion reactor, *Phys. Rev. Lett.* **43** 1318 (1979).

4 R F Post, The magnetic mirror approach to fusion, *Nucl. Fusion* **27** 1579 (1987).

5 D E Baldwin, End-loss processes from mirror machines, *Rev. Mod. Phys.* **49** 317 (1977).

6 V P Pastukhov, Collisional losses of electrons from an adiabatic trap in a plasma with a positive potential, *Nucl. Fusion* **14** 3 (1974).

7 R F Post and M N Rosenbluth, Electrostatic instabilities in finite mirror-confined plasmas, *Phys. Fluids* **9** 730 (1966).

8 N J Fisch and J-M Rax, Interaction of energetic alpha particles with intense lower hybrid waves, *Phys. Rev. Lett.* **69** 612 (1992).

9 N J Fisch, Theory of current drive in plasmas, *Rev. Mod. Phys.* **59** 175 (1987).

10 R W Moir and W L Barr, Venetian-blind direct energy converter for fusion reactors, *Nucl. Fusion* **13** 35 (1973).

11 W L Barr and R W Moir, Test results on plasma direct converters, *Nucl. Technol./Fusion* **3** 98 (1983).

12 D P Grubb *et al*, Thermal-barrier production and identification in a tandem mirror, *Phys. Rev. Lett.* **53** 783 (1984).

13 T Cho *et al*, Observation of the effects of radially sheared electric fields on the confinement in the GAMMA 10 tandem mirror, *Phys. Rev. Lett.* **94** 085002 (2005).

14 D Endrizzi *et al*, Physics basis for the Wisconsin HTS Axisymmetric Mirror (WHAM), *J. Plasma Phys.* **89** 975890501 (2023).

15 D D Ryutov, H L Berk, B I Cohen, A W Molvik and T C Simonen, Magneto-hydrodynamically stable axisymmetric mirrors, *Phys. Plasmas* **18** 092301 (2011).

16 L L Lao, H St John, R D Stambaugh, A G Kellman and W Pfeiffer, Reconstruction of current profile parameters and plasma shapes in tokamaks, *Nucl. Fusion* **25** 1611 (1985). doi:10.1088/0029-5515/25/11/007

17 A Pironti and M Walker, Fusion, tokamaks, and plasma control: an introduction and tutorial, *IEEE Control Syst. Mag.* **25**(5) 30 (2005). doi:10.1109/MCS.2005.1512794

18 F Felici *et al*, Real-time physics-model-based simulation of the current density profile in tokamak plasmas, *Nucl. Fusion* **51** 083052 (2011). doi:10.1088/0029-5515/51/8/083052

19 O Meneghini *et al*, Integrated modeling applications for tokamak experiments with OMFIT, *Nucl. Fusion* **55** 083008 (2015). doi:10.1088/0029-5515/55/8/083008

20 J Degrave *et al*, Magnetic control of tokamak plasmas through deep reinforcement learning, *Nature* **602** 414 (2022). doi:10.1038/s41586-021-04301-9

21 J Kates-Harbeck, A Svyatkovskiy and W Tang, Predicting disruptive instabilities in controlled fusion plasmas through deep learning, *Nature* **568** 526 (2019). doi:10.1038/s41586-019-1116-4

22 D Q Mayne, J B Rawlings, C V Rao and P O M Scokaert, Constrained model predictive control: stability and optimality, *Automatica* **36** 789 (2000).

23 A Bemporad, M Morari, V Dua and E N Pistikopoulos, The explicit linear quadratic regulator for constrained systems, *Automatica* **38** 3 (2002).

24 E G Gilbert and I Kolmanovsky, Nonlinear tracking control in the presence of state and control constraints: a generalized reference governor, *Automatica* **38** 2063 (2002).

25 A D Ames, X Xu, J W Grizzle and P Tabuada, Control barrier function based quadratic programs for safety critical systems, *IEEE Trans. Autom. Control* **62** 3861 (2017).

26 L Lu, P Jin, G Pang, Z Zhang and G E Karniadakis, Learning nonlinear operators via DeepONet based on the universal approximation theorem of operators, *Nat. Mach. Intell.* **3** 218 (2021). doi:10.1038/s42256-021-00302-5

27 Z Li, N Kovachki, K Azizzadenesheli, B Liu, K Bhattacharya, A Stuart and A Anandkumar, Fourier neural operator for parametric partial differential equations, *Int. Conf. on Learning Representations (ICLR)* (2021). arXiv:2010.08895

28 M Raissi, P Perdikaris and G E Karniadakis, Physics-informed neural networks: a deep learning framework for solving forward and inverse problems involving nonlinear partial differential equations, *J. Comput. Phys.* **378** 686 (2019). doi:10.1016/j.jcp.2018.10.045

29 K L van de Plassche, J Citrin, C Bourdelle *et al*, Fast modeling of turbulent transport in fusion plasmas using neural networks, *Phys. Plasmas* **27** 022310 (2020). doi:10.1063/1.5134126

30 J E Menard *et al*, Fusion nuclear science facilities and pilot plants based on the spherical tokamak, *Nucl. Fusion* **56** 106023 (2016). doi:10.1088/0029-5515/56/10/106023

31 A J Creely *et al*, Overview of the SPARC tokamak, *J. Plasma Phys.* **86** 865860502 (2020). doi:10.1017/S0022377820001257

32 M G Kapteyn, J V R Pretorius and K E Willcox, A probabilistic graphical model foundation for enabling predictive digital twins at scale, *Nat. Comput. Sci.* **1** 337 (2021). doi:10.1038/s43588-021-00069-0

33 P I Ford, *Kronos Physics De-Risking Register*, Kronos Fusion Energy 2026 series. doi:10.5281/zenodo.22133057

COLOPHON

How this document was made

The Kronos Fleet — Combined Editorial, 2026 is set in **Fraunces** (display), **Gelasio** (text), and **IBM Plex Mono** (data & equations), carried forward from the Kronos editorial design system.

The figures are rendered at 300 dpi from the deposited generator scripts; the document is composed as a single self-contained file with embedded fonts and imagery, paginated to US Letter, and rendered to PDF through a headless Chromium engine in matched light and dark editions.

Every headline quantity carries an evidence class; withdrawn and restated values are marked as such. Nothing herein is frozen beyond the founder-approved Tier-A set.

Explore it live — turn the interactive 3-D model, run the deposited solvers in the physics validator, and watch the companion film series.

LEGAL NOTICE

Notice, status, and distribution

Conceptual design & simulation study. This document reports a conceptual design and simulation study. It is not a construction commitment, a safety-analysis report, a regulatory filing, or an offer of securities. Forward-looking statements — schedules, costs, market sizes, and performance — are estimates subject to the limitations set out in the Simulations part and may change.

Numbers and their classes. Quantities are reported with evidence classes and case labels; modelled, assumed, and requirement-class values are identified as such and are not to be quoted without their labels.

Public edition. This edition carries the physics and design only; all financial, funding, and defense-commercial content has been removed for public distribution. The scientific text corresponds to the arXiv and journal submissions.

THE 2026 KRONOS SERIES

One programme, many papers

This editorial is one paper in the Kronos 2026 series — a real fusion company's complete, reproducible physics record for a spherical-tokamak breeder and its low-neutron D–^{3}He tandem-mirror burners. Every headline number is a frozen anchor in the Physics De-Risking Register.

Explore the whole programme: the De-Risking Register, the interactive 3-D model, and the physics validator.

KRONOS FUSION ENERGY

A Real-Time Control Suite for a D-3He Tandem-Mirror Burner: Plug-Potential, Sloshing-Ion, DCLC/AIC-Microstability, and Direct-Energy-Converter Dispatch Controllers

A real fusion company building real machines. Explore the science, live.

Zenodo · doi:10.5281/zenodo.22645811

Read on kronosfusionenergy.com

The Physics De-Risking Register